# Vortical Flow over an Elliptical-Body Missile at High Angles of Attack

Richard W. Newsome*
*NASA Langley Research Center, Hampton, Virginia*
and
Mary S. Adams†
*NASA Langley Research Center, Hampton, Virginia*

**Numerical solutions to the Reynolds-averaged Navier-Stokes equations are given for the flow about an elliptical body missile (3:1 ellipse) at a Mach number of 2.5 and a Reynolds number of $4.66 \times 10^6$ based on body length. At high angles of attack, the flow is dominated by large-scale free vortices that occur in the leeside flowfield due to crossflow boundary-layer separation. Emphasis is focused on the accurate prediction of the leeside vortical flow. Solutions are presented for both symmetric and asymmetric (body rolled 45 deg) configurations at 10 and 20 deg angles of attack. The computed results are compared with experimental surface pressure measurements and vapor-screen photographs. Excellent agreement is obtained in all cases.**

## Introduction

THE viscous flow about aircraft and missiles at high angles of attack is characterized by three-dimensional boundary-layer separation and the presence of large free vortices in the leeside flowfield. This flight regime, typical of off-design and maneuvering conditions, has assumed additional importance in efforts to enlarge the allowable flight envelope. Traditional analysis methods, which are appropriate for attached flow, are not applicable in this flow regime. Solutions to the Reynolds-averaged Navier-Stokes equations are necessary to describe the physics of the flow adequately. However, demands on computer memory and CPU time have severely limited the application of such methods to realistic problems. The advent of high-speed vector-processor computers has significantly increased the complexity of problems that can now be addressed. The intent of the present effort is to study the symmetric and asymmetric vortex shedding over an elliptical-body missile at high angles of attack through numerical solution of the Reynolds-averaged Navier-Stokes equations on the NASA Langley Research Center VPS 32 (Cyber 205) computer.

As opposed to the more conventional circular missile cross section, the elliptical cross section offers several potential advantages. It provides a higher ratio of normal to side force and more favorable out-of-plane forces and moments than an equivalent missile with a circular cross section.[1] This leads to better compatibility in longitudinal directional stability.[2] At moderate to high angles of attack, both cross sections are dominated by the vortices in the leeward flow. The vortices induce a lower pressure on the leeward body surface, which results in an additional normal force component not predicted by linear theory. When the vortices are stable and symmetric, the vortical flow may be exploited to acrodynamic advantage. For the elliptic cross section, most of the normal force is, in fact, developed by the body rather than by the tail or wings. Thus, an accurate prediction of the vortical flow over the body is essential if reasonable forces and moments are to be calculated for the overall missile. However, the nature of the separation and the location of the separation lines are known only when the boundary layer is integrated up to and through the point of separation. A further complication occurs at nonzero roll angle (or an equivalent yaw angle) where the elliptical cross section produces highly asymmetric vortices.

Sharp and blunt-nosed elliptical cross-sectional missiles were extensively tested in the NASA Langley Unitary Plan Wind Tunnel for body alone, body-wing-tail, and body-tail configurations at a variety of angles of attack and roll angle in order to form a database for comparison with computational methods.[3] In the range of angles of attack considered ($-5$ to 25 deg), the vortices were quasisteady and symmetric (at zero roll angle), and vortex bursting, asymmetric vortices, and unsteady vortex shedding were not observed. The onset of these phenomena defines the upper limit in which the vortical flow may be favorably exploited in efforts to enlarge the performance envelope.

Reference 4 describes the evaluation of a number of approximate computational methods for the sharp-nosed elliptical body missile. These include a full potential method,[5] a vortex cloud method[6] in which the vortex is represented as a set of discrete point vortices, and a supersonic/hypersonic arbitrary body program (S/HABP)[7] for predicting surface pressure. In general, satisfactory results were not reported. The potential method was incapable of representing the crossflow separation

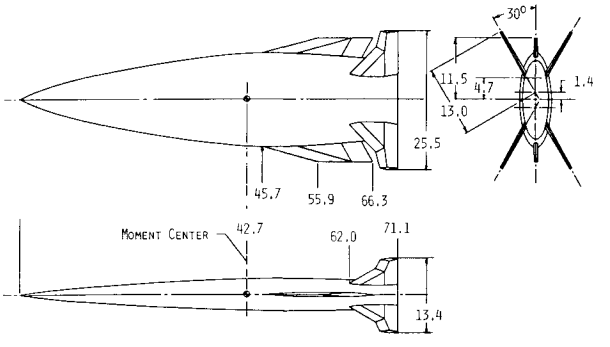


**Fig. 1 Elliptical body missile (all dimensions in cm).**

Presented as Paper 86-0559 at the AIAA 24th Aerospace Sciences Meeting, Reno, NV, Jan. 6-9, 1986; received May 22, 1987; revision received Feb. 2, 1987. 

*Major, U.S. Air Force. Air Force Wright Aeronautical Laboratories. Member AIAA.

†Data Analyst, Computational Methods Branch, High-Speed Aerodynamics Division.

and the resulting vortex structure that is the dominant flow characteristic. The discrete vortex method only crudely modeled the actual vortical flow with equally poor results. The S/HABP program was the least exact of the methods reported. Euler calculations[8] resulted in inviscid separation due to the spurious generation of vorticity in the crossflow expansion. The coupling of three-dimensional boundary layer and Euler codes in a region of strong viscous-inviscid interaction is a difficult procedure that, at best, can only determine the primary separation line and establish the primary vortex through an enforced Kutta condition at the point of separation. The Navier-Stokes equations are not limited by the restrictions of the more approximate methods and, with the advent of computers such as the Cyber 205, the solution of the three-dimensoinal Navier-Stokes equations for body, wing-body, or wing-body-tail configurations is now a reasonable calculation. The goal of the present Navier-Stokes calculations is twofold: 1) produce quantitatively valid solutions that compare favorably with experiment and 2) provide an enhanced qualitative understanding of the flow through post-processing graphics.

## Theory

The governing equations are the compressible three-dimensional Reynolds (mass)-averaged Navier-Stokes equations written in conservative form in the transformed coordinate system. Inflow boundary conditions were fixed as the conical solution to the governing equations at a station near the apex of the sharp-nosed body using a previously developed conical flow code.[9,10] The outer boundary was placed outside the bow shock so that freestream conditions could be prescribed. On the body surface, the no-slip conditions were applied. Surface pressure was determined by the simplified normal momentum equation (pressure extrapolation). Surface temperature was specified as the adiabatic wall temperature based on freestream conditions. A symmetry condition was applied through reflection about the centerline plane for the symmetric flow at 0 deg roll angle. For the asymmetric calculations at 45 deg roll angle, a periodic boundary condition was applied on the windward centerline plane with a two-point mesh overlap. Since the outflow was supersonic, the conservative variables were extrapolated at the outflow boundary.

Turbulent closure was provided by a modified Baldwin-Lomax[11] turbulence model. The Baldwin-Lomax model is a two-layer (inner/outer) eddy viscosity model. The baseline model performs well in regions of attached flow but breaks down in regions of large crossflow separation. The basic problem is determining the proper length and velocity scales in the vortical flow on the lee side of the body. The model scales the outer eddy viscosity according to the maximum value of a function that is proportional to the vorticity magnitude in the profile normal to the body surface. The baseline model thus scales the outer eddy viscosity relative to the vorticity maximum in the leeside vortex core, rather than the smaller local maximum in the boundary layer beneath the vortex. The outer eddy viscosity is then too large, and the net effect is to distort the flow by decreasing the size of the primary vortex, changing the location of the separation lines, and even suppressing the secondary vortices. This situation is discussed by Degani and Schiff[12] together with appropriate modifications. The modifications adopted here, similar to those proposed in Ref. 12, ensure that the outer eddy viscosity is correctly scaled relative to the leeside boundary layer rather than the vortex core.

The three-dimensional grid was generated as a series of planar surfaces. Each grid surface was obtained by the method of Thompson et al.[13] as the solution of two Poisson equations. The resulting grid is smooth and nearly orthogonal to the body.

MacCormack's unsplit, explicit finite-difference algorithm[14] was used to obtain numerical solutions. The method is second-order accurate in space and time and is conditionally stable. Additional efficiency was achieved by the use of a local stability bound with a time-step limit set as a multiple of the global minimum time step. MacCormack's pressure damping was used to control shock oscillations. Kumar's three-dimensional inlet code[15] was adapted to solve the external flow about the missile. The code is a highly vectorized MacCormack algorithm implemented in half-precision (32-bit) arithmetic. The vector length corresponds to the product of the two crossflow plane indices. The use of 32-bit arithmetic doubles the execution speed of vector statements that make up virtually the entire code while halving the necessary storage. The convergence achieved with 32-bit arithmetic is quite adequate for engineering calculations. For the largest grid considered, $35 \times 101 \times 61$ (215,635) points, a converged solution required roughly two hours of CPU time at a data processing rate of $1.02 \times 10^{-5}$ CPU seconds/grid point/iteration and required 2.5 M 64-bit words of memory.

Limiting streamlines defines a velocity field adjacent to the body surface that exists for any finite height of the streamlines above the surface. In the limit, as the height approaches zero, the streamlines become parallel to the body surface and are coincident with the skin friction lines or surface shear stress trajectories.[16,17] Experimentally, skin friction lines are realized through oil-streak flow visualization. Topological rules, based on the number and type of singularities in the vector field defined by skin friction lines, have been devised to interpret and explain oil-flow results for three-dimensional separated flows. In the present case, it is sufficient to note that the conver-

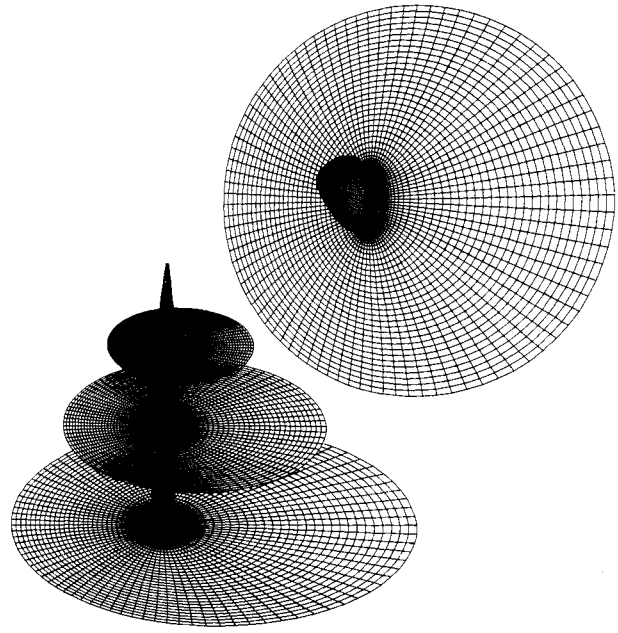

**Fig. 2 Grid, $\alpha = 10$ deg, $\beta = 0$ deg (grid reflected about symmetry plane).**

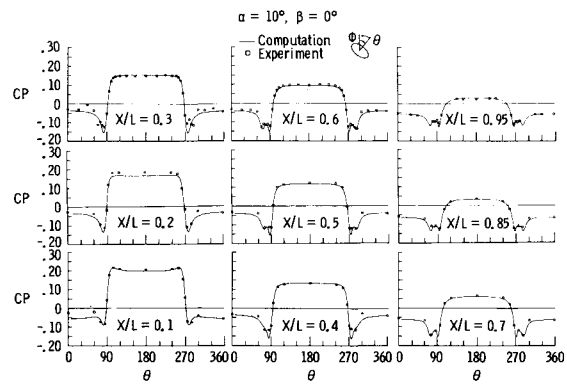


**Fig. 3 Surface pressure coefficient, Mach = 2.5, $\alpha = 10$ deg, $\beta = 0$ deg.**

gence of skin friction lines indicates a line of separation, whereas divergence indicates a line of reattachment. Limiting streamlines (or skin friction lines) can be determined numerically. The projection of the velocity field adjacent to the body surface onto the surface is given by

$$\boldsymbol{U}_p = (u_p, v_p, w_p) = \boldsymbol{U} - (\hat{N}_s \cdot \boldsymbol{U})\hat{N}_s \tag{1}$$

where $\hat{N}_s$ is the outward body normal and $\boldsymbol{U}$ is the velocity one point away from the wall. The solution of the two kinematic equations relating the coordinates $\xi$ and $\eta$ on the body surface, $\zeta = 0$, to the projected contravariant velocity components, $(U_c, V_c)$,

$$\xi_t = U_c = \xi_x u_p + \xi_y u_p + \xi_z w_p$$
$$\eta_t = V_c = \eta_x u_p + \eta_y u_p + \xi_z w_p \tag{2}$$

define the skin friction lines. Equation (2) is then integrated in the uniform computational grid and interpolated to define the particle path (skin friction line) in physical coordinates $(x, y, z)$. In the results to follow, a new path line is initiated at each of the surface grid-point locations. The trajectory is terminated when the next crossflow grid station is encountered. When combined with crossflow velocity vector plots, the computed skin friction lines clearly reveal both separation and reattachment lines.

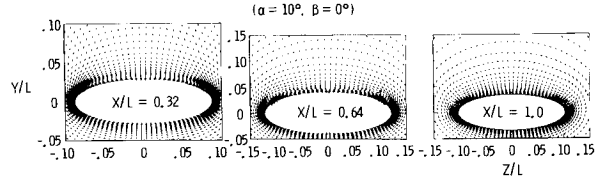


**Fig. 4 Crossflow velocity vectors, Mach = 2.5, $\alpha$ = 10 deg, $\beta$ = 0 deg.**

## Results

A three-view drawing of the sharp-nosed, elliptical body missile is shown in Fig. 1. Since interest was focused on the development of the leeside vortical flow as a result of crossflow boundary-layer separation on the body, calculations were performed for the body-alone configuration and compared with corresponding experimental data. Experimental test conditions were

$$M_\infty = 2.5 \quad T_{T_\infty} = 339°\text{K}$$
$$P_{T_\infty} = 81.36\ \text{KPa} \quad Re_{\infty_L} = 4.66 \times 10^6$$

Grit was applied to the body at $x/L = 0.043$ ($L = 71.1$ cm) to induce boundary-layer transition. The computations performed are shown in Table 1.

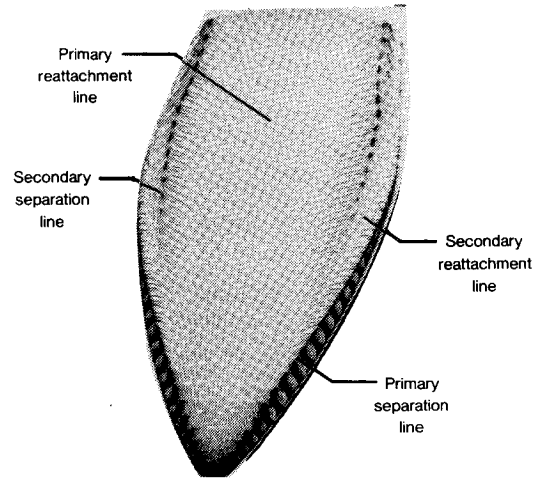


**Fig. 6 Skin friction lines, Mach = 2.5, $\alpha$ = 10 deg, $\beta$ = 0 deg.**

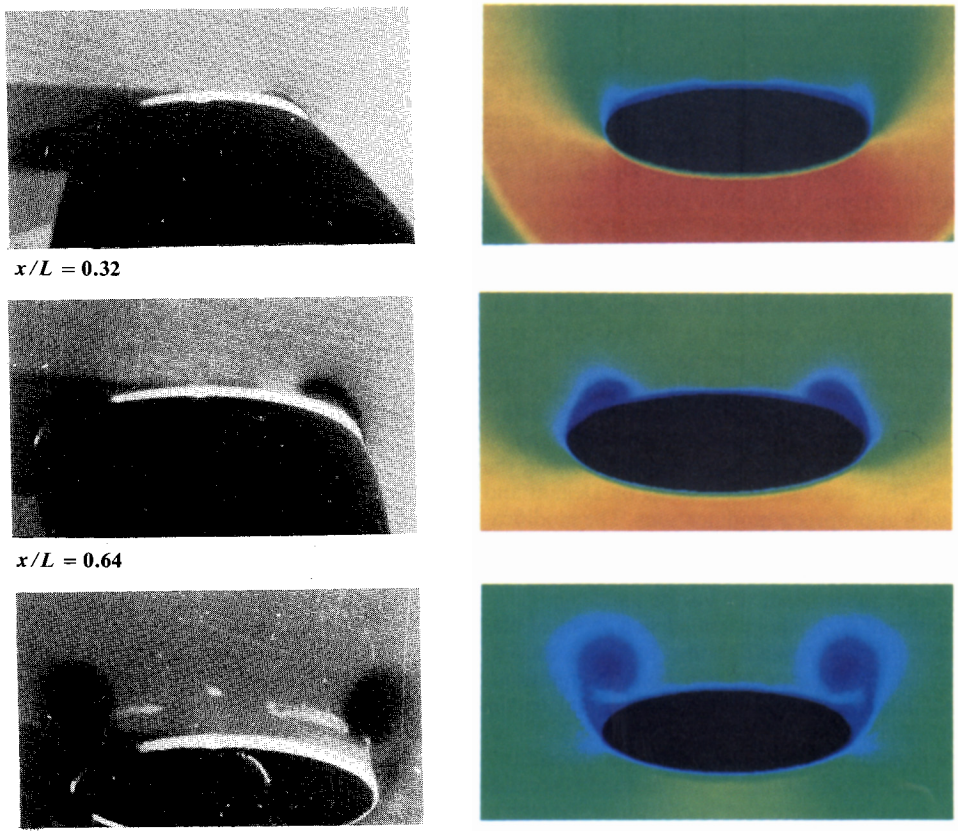

$x/L$ = 0.32

$x/L$ = 0.64

$x/L$ = 1.0

**Fig. 5 Comparison of experimental vapor screen and computed density field, Mach = 2.5, $\alpha$ = 10 deg, $\beta$ = 0 deg.**

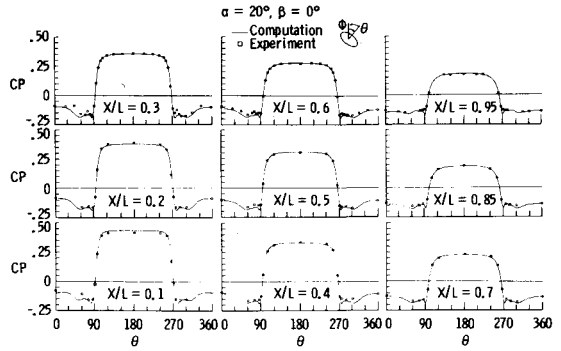


**Fig. 7 Surface pressure coefficient, Mach = 2.5, $\alpha = 20$ deg, $\beta = 0$ deg.**

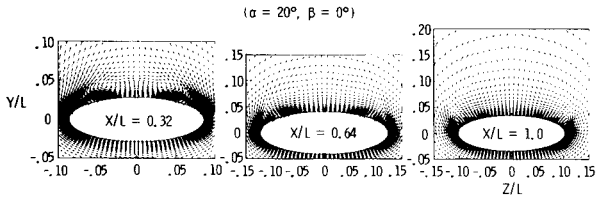


**Fig. 8 Crossflow velocity vectors, Mach = 2.5, $\alpha = 20$ deg, $\beta = 0$ deg.**

**Table 1**

| Case | Angle of attack, deg | Roll angle, deg |
|---|---|---|
| 1 | 10 | 0 (symmetric) |
| 2 | 20 | 0 (symmetric) |
| 3 | 10 | 45 (asymmetric) |
| 4 | 20 | 45 (asymmetric) |

## Symmetric Flow

The three-dimensional grid used for the 10 deg angle of attack, 0 deg roll angle is shown in Fig. 2. The upstream surface was set at a distance $x/L = 0.025$. The conical Navier-Stokes equations were then solved for an equivalent conical elliptical body that matched the slopes of the major and minor axes $(a_x, b_x)$ at the specified station. Since the boundary layer was tripped just downstream of this station, the entire flow, including the conical starting solution, was assumed to be turbulent. In all cases, the minimum spacing adjacent to the wall in the windward (attached) boundary layer was set at a nondimensional law-of-the-wall distance of $s^+ = 10$. In the leeside vortical flow, this same minimum spacing resulted in a value $s^+ \leq 5$. The grid for the 10 deg angle-of-attack case consisted of 32 points along the body ($\xi$) length, 46 points around the body ($\eta$), and 48 points outward from the body ($\zeta$). The windward boundary layer was spanned by roughly 8 points at inflow and 16 points at outflow.

A comparison of surface pressure coefficients is shown in Fig. 3. The computed results have been reflected about the symmetry plane for comparison with the 360 deg experimental results. The degree of asymmetry in the experimental results provides a measure of experimental error. At the earlier stations, $x/L = 0.3 - 0.5$, the experimental results indicate that crossflow boundary-layer separation occurs somewhat earlier (more windward) than the computed results. Since the adverse pressure gradient is rather mild, the precise point of separation is critically dependent on the computed eddy viscosity coefficient. The neglect of any transition region with the assumption of fully turbulent flow at inflow may serve to delay separation. At the latter stations, excellent agreement was found on both the windward and leeward surfaces. Crossflow velocity is given at three of the four stations, corresponding to the location of the experimental vapor-screen photographs in Fig. 4. At the station $x/L = 0.32$, the crossflow has separated but a well-defined vortex is not yet evident. At the station $x/L = 0.64$, the primary vortex is evident. Secondary separa-

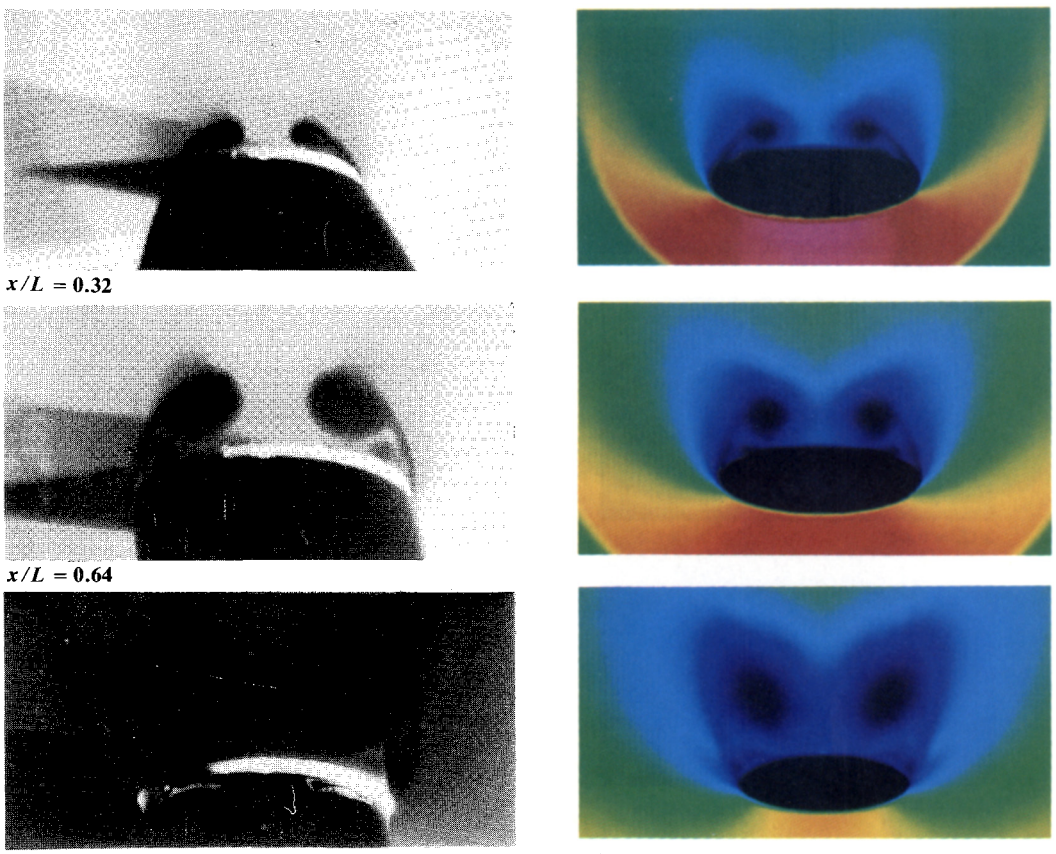

$x/L = 0.32$ $x/L = 0.64$ $x/L = 0.89$ $x/L = 1.0$

**Fig. 9 Comparison of experimental vapor screen and computed density field, Mach = 2.5, $\alpha = 20$ deg, $\beta = 0$ deg.**

tion is incipient at this station. At the last station, $x/L = 1.0$, the core of the primary vortex has moved away from the surface. The secondary vortex is also evident, and a tertiary vortex can be seen between the secondary reattachment line and the primary separation line in which flow from the primary separation is entrained into this tertiary vortex. Experimental vapor-screen photographs were taken at the stations $x/L = 0.32$, 0.64, 0.89, and 1.0. A color graphics representation of the density at the stations $x/L = 0.32$, 0.64, and 1.0 is compared with the vapor-screen results in Fig. 5. The vortices appear as dark blue to black, corresponding to the lowest density regions on the color scale. There is a striking similarity in the size and shape of the computed and experimental vortices. Skin friction lines are shown in Fig. 6. The primary separation line originates at the upstream boundary and moves more windward as it traverses the body length. The secondary separation line first appears at $x/L = 0.49$, and the secondary attachment line occurs just downstream of this point.

The grid for 20 deg angle of attack was similar to the 10 deg case. It consisted of 33 points along the body, 51 points around the body, and 57 points outward from the body. The minimum step size and boundary-layer resolution criteria were similar to the 10 deg angle-of-attack case. The computed surface pressure coefficient, Fig. 7, is in excellent agreement with experiment. In contrast to the 10 deg case, the separation is clearly established at the inflow plane and is less dependent on the eddy viscosity predicted by the turbulence model. As a result, the surface pressure coefficient on the leeward surface is accurately predicted even at the upstream stations. Crossflow velocity plots are given in Fig. 8. The vortical flow is much more obvious than in the 10 deg case. Both primary and secondary vortices are apparent at the stations $x/L = 0.32$ and 0.64. At the last station, $x/L = 1.0$, the primary vortex core had lifted off the body and became rather elliptical in shape. The two counter-rotating secondary/tertiary vortices previously noted at this station in the 10 deg case were again present. Vapor-screen photographs and the computed density field are compared in

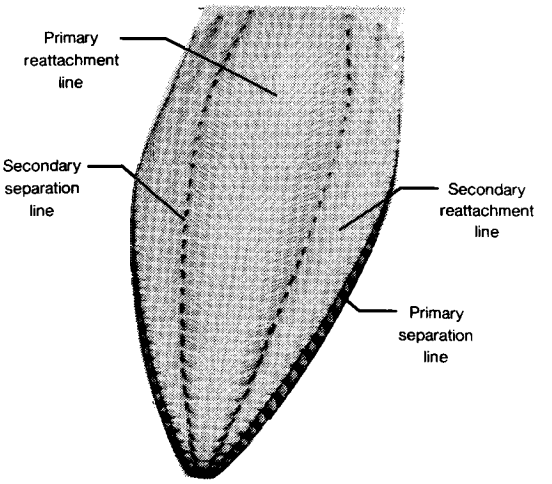


**Fig. 10 Skin friction lines, Mach = 2.5, $\alpha$ = 20 deg, $\beta$ = 0 deg.**

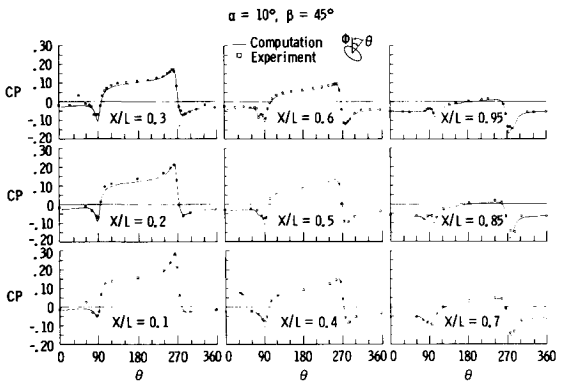


**Fig. 11 Surface pressure coefficient, Mach = 2.5, $\alpha$ = 10 deg, $\beta$ = 45 deg.**

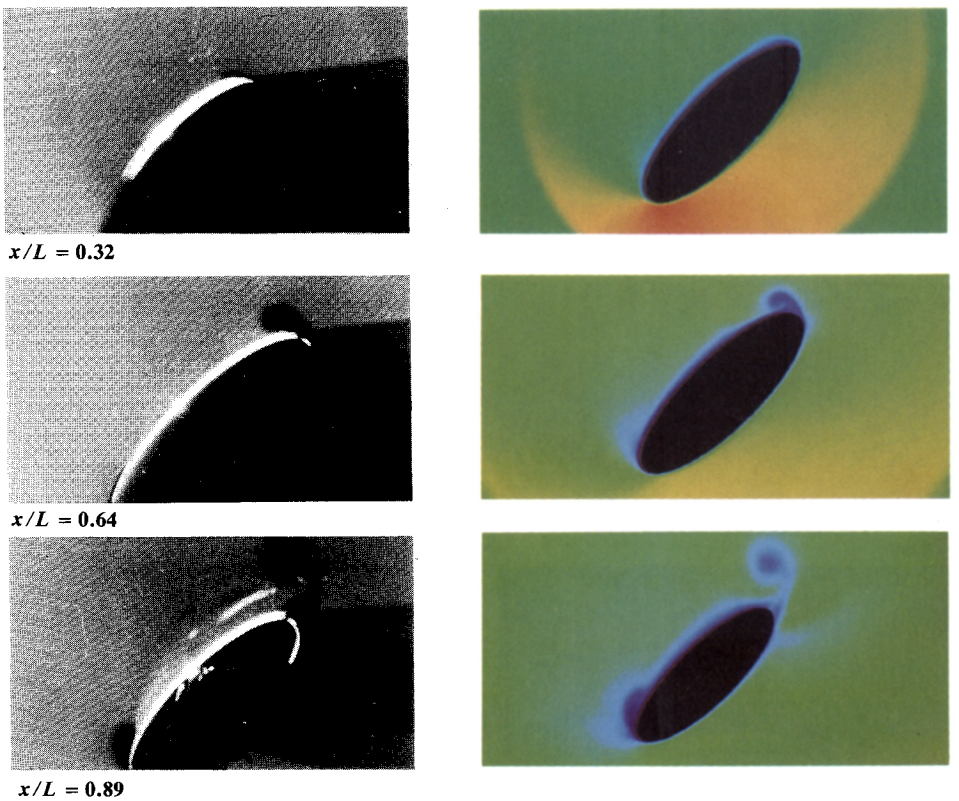


**Fig. 12 Comparison of experimental vapor screen and computed density fields, Mach = 2.5, $\alpha$ = 10 deg, $\beta$ = 45 deg.**

Fig. 9. Since the vapor-screen photograph was not available at $x/L = 1.0$, the result at $x/L = 0.89$ has been substituted instead. Skin friction lines are shown in Fig. 10. Both the primary and secondary separation and reattachment lines are established at inflow and run the length of the body.

## Asymmetric Flow

The grid used in the asymmetric flow calculation at 10 deg angle of attack, 45 deg angle was composed of 35 points along the body, 51 outward from the body, and 101 points around the body with a two-point mesh overlap. The surface pressure coefficient for this case is given in Fig. 11. As in the symmetric case at 10 deg angle of attack, separation on the leeward edge occured sooner than the computation predicted at the upstream stations, $x/L = 0.3 - 0.5$. A comparison of the vapor-screen and a color graphics representation of the computed density field is given in Fig. 12. The flow on the windward edge remains attached at $x/L = 0.32$ and 0.64 whereas separation is evident at the last station, $x/L = 1.0$. On the leeward side, the primary vortex can be seen at $x/L = 0.64$. At $x/L = 1.0$, the primary vortex is displaced from the body, and the characteristic secondary/tertiary vortices appear under the primary vortex. The computed skin friction lines (not shown) indicate that the windward separation line first appears at $x/L = 0.78$. On the leeward side, a primary separation line runs along the entire body length, whereas the secondary separation and reattachment lines begin much further downstream at a distance $x/L = 0.62$.

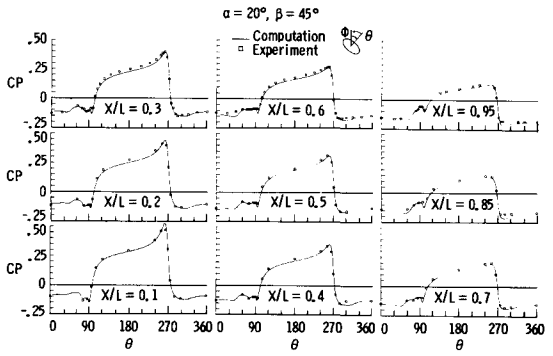


**Fig. 13 Surface pressure coefficient, Mach = 2.5, $\alpha = 20$ deg, $\beta = 45$ deg.**

Grid dimensions for the 20 deg angle-of-attack asymmetric flow case were 35 points along the body, 101 points around the body, and 61 points outward from the body. The computed surface pressure coefficient, Fig. 13, exhibits excellent agreement with experiment along the entire body length on the windward and leeward sides. A comparison of the vapor-screen photographs with the computed density flowfield is given in Fig. 14. The predicted location and size of the vortices are in agreement with the experimental results. The flow on the windward edge remains attached, and separation and reattachment occur near the mid-body position. The windward vortex is quite strong and remains very close to the body surface. A crossflow shock is evident above this vortex in both the vapor-screen and the computation. In moving downstream, the computed skin friction lines (not shown) indicate that the primary separation line moves progressively toward the windward edge, whereas the vortex core moves toward the leeward edge. At the last station, $x/L = 1.0$, the vortex extends virtually from the windward edge to the leeward edge. The leeward vortex is much weaker and is shed into the flow at some distance above the body. At $x/L = 0.32$, the leeward secondary separation is insipient, and at $x/L = 0.64$, the leeward secondary vortex is visible. At the last station, $x/L = 1.0$, the windward and leeward vortices interact to produce the two counterrotating vortices previously noted at this station.

## Conclusions

Numerical solutions to the Reynolds-averaged Navier-Stokes equations for the turbulent flow about an elliptical body

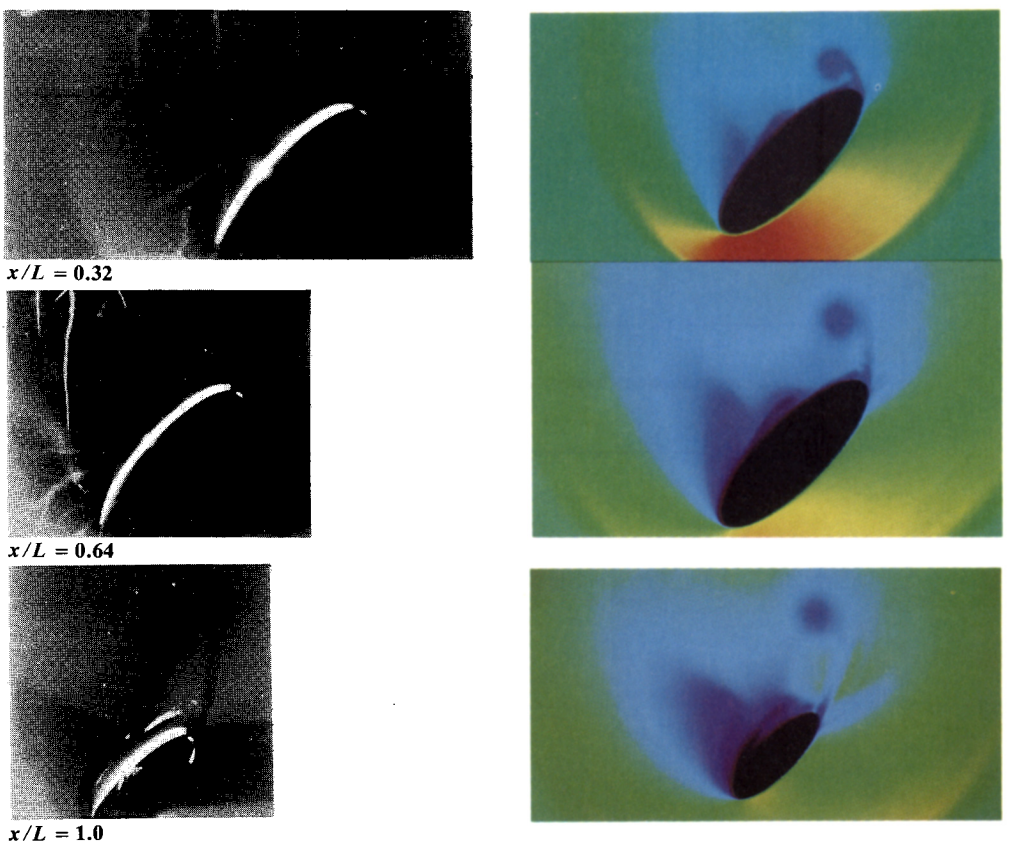


**Fig. 14 Comparison of experimental vapor screen and computed density fields, Mach = 2.5, $\alpha = 20$ deg, $\beta = 45$ deg.**

missile at a Mach number of 2.5 and a Reynolds number of $4.66 \times 10^6$ have been presented for angles of attack of 10 and 20 deg at roll angles of 0 and 45 deg. Very good agreement with the experimental surface pressure measurements is shown in all four cases. A comparison of the color graphics representation of the density at several stations with corresponding experimental vapor-screen photographs demonstrates that the calculation successfully predicts the size, shape, and location of the vortices that dominate the leeward flowfield. Finally, crossflow velocity plots and skin friction lines are used to delineate the vortical structure due to crossflow boundary-layer separation and the accompanying separation and reattachment lines.

The present results indicate that quantitatively valid solutions can be obtained with a simple algebraic turbulence model for the vortical flow about the elliptical body missile. The solutions may be obtained in a reasonably efficient manner using present-day vector-processor computers. When combined with effective graphics, the numerical solutions provide an enhanced qualitative understanding as well.

## References

[1]Gregoriou, G., "Modern Missile Design for High Angle of Attack," *High Angle of Attack Aerodynamics*, AGARD Lecture Series No. 121, March 1982, pp. 5.1–5.23.

[2]Graves, E. B., "Aerodynamic Characteristics of a Monoplanar Missile Concept with Bodies of Circular and Elliptical Cross Sections," NASA TM-74079, 1977.

[3]Allen, J. M., Hernandez, G., and Lamb, M., "Body-Surface Pressure Data on Two Monoplane-Wing Missile Configurations with Elliptical Cross Sections at Mach 2.5," NASA TM-85645, 1985.

[4]Allen, J. M. and Pittman, J. L., "Analysis of Surface Pressure Distributions on Two Elliptic Missile Configurations," AIAA Paper 83-1841, July 1983.

[5]Siclari, M. J., "The NCOREL Computer Program for 3-D Nonlinear Potential Flow Computations, NASA CR 3694, 1983.

[6]Mendenhall, M. R. and Perkins, S. C., "Prediction of Vortex Shedding from Circular and Noncircular Bodies in Supersonic Flow," NASA CR-3754, Jan. 1984.

[7]Gentry, A. E., Smyth, D. N., and Oliver, W. R., "The Mark IV Supersonic-Hypersonic Arbitrary Body Program Formulation," Vol. III, AFFDL TR-73-159, Nov. 1973.

[8]Allen, J. M. and Townsend, J. C., "Application of the SWINT Code to Wing-Body-Tail Geometries," AIAA Paper 85-1811, Aug. 1985.

[9]Newsome, R. W., "Euler and Navier-Stokes Solutions for Flow Over a Conical Delta Wing, " *AIAA Journal*, April 1986, Vol. 4, pp. 552–561.

[10]Newsome, R. W. and Thomas, J. L., "Computation of Leading-Edge Vortex Flows," NASA CP-2416, Oct. 1985, pp. 305–330.

[11]Baldwin, B. S. and Lomax, H., "Thin Layer Approximation and Algebraic Model for Separated Turbulent Flows," AIAA Paper 78-257, Jan. 1978.

[12]Degani, D. and Schiff, L. B., "Computation of Supersonic Viscous Flows Around Pointed Bodies at Large Incidence," AIAA Paper 83-0034, Jan. 1983.

[13]Thompson, J. F., Thames, F. C., and Mastin, C. W., "Boundary Fitted Coordinate Systems for Solution of Partial Differential Equations on Fields Containing Any Number of Arbitrary Two-Dimensional Bodies," NASA CR-2729, July 1977.

[14]MacCormack, R. W., "The Effect of Viscosity in Hypervelocity Impact Cratering," AIAA Paper 69-354, 1969.

[15]Kumar, A., "Numerical Analysis of the Scramjet Inlet Flow Field Using the Three-Dimensional Navier-Stokes Equations," *CPIA Publication 373*, Feb. 1983, pp. 25–29.

[16]Peake, D. J. and Tobak, M., "Three-Dimensional Separation and Reattachment," *High Angle of Attack Aerodynamics*, AGARD Lecture Series No. 121, March 1982, pp. 1.1–1.14.

[17]Peake, D. J. and Tobak, M., "Three-Dimensional Interactions and Vortical Flows With Emphasis on High Speeds," AGARDograph No. 252, July 1980.

**Color reproduction courtesy of NASA Langley Research Center.**